THESIS FOR THE LICENTIATE DEGREE OF ENGINEERING

Proton Conducting Ceramics; Synthesis, Characterization and Sample Cell Environments

KINYANJUI G. FRANCIS

Department of Chemical and Biological Engineering

CHALMERS UNIVERSITY OF TECHNOLOGY

Göteborg, Sweden 2012

Proton Conducting Ceramics; Synthesis, Characterization and Sample Cell Environments

KINYANJUI G. FRANCIS

Licentiatuppsatser vid Institutionen för kemi- och bioteknik

Chalmers tekniska högskola

Serial no: 2012:14

ISSN: 1652-943X

Department of Chemical and Biological Engineering

Chalmers University of Technology

SE-412 96 Göteborg

Sweden

Telephone + 46 (0)31-772 1000

Cover: The deuteron position (green) and its associated bond distances (Å) within the unit cell of $BaSn_{0.6}Sc_{0.4}O_{2.8}(D_2O)_{0.2}$.

Printed at Chalmers Reproservice AB

Göteborg, Sweden 2012

To my wife and Family

”Mgaagaa na upwa hali wali mkavu”.

A swahili proverb

Proton Conducting Ceramics; Synthesis, Characterization and Sample Cell Environments

Kinyanjui G. Francis

Department of Chemical and Biological Engineering

Chalmers University of Technology

ABSTRACT

Acceptor doped Perovskite ceramics have been shown to exhibit high levels of protonic conduction in humid atmospheres. However significant grain boundary resistance and long sintering times required to achieve sufficient grain size growth has hindered their widespread application as electrolyzers, fuel cells and gas separation membranes. Furthermore there is insufficient detailed knowledge on the local environment of the H^+ and its behavior in relation to the crystal structure under real working conditions.

The works of the thesis describe the synthesis, structural characterization and conductivity of $BaZr_{0.5}In_{0.5}O_{3-\delta}$ and $BaSn_{1-x}Sc_xO_{3-\delta}$ (x = 0, 0.1, 0.2, 0.3, 0.4, 0.5). Traditional solid state sintering was used to prepare the samples which were then characterized by a variety of methods such as electrochemical impedance spectroscopy, thermogravimetric analysis, X-ray and neutron diffraction. Spark plasma sintering processing technique has been explored.

$BaZr_{0.5}In_{0.5}O_{3-\delta}$ processed using the spark plasma sintering method were found to exhibit higher grain boundary conductivity compared to solid state sintered samples that had fewer grain boundaries under wet H_2 (5% H_2 + 95% Ar). The highest proton conductivity was found in the SPS samples under wet H_2 atmosphere.

In $BaSn_{1-x}Sc_xO_{3-\delta}$ the deuteron was found to occupy the 24*k* crystallographic position by Rietveld analysis of room temperature neutron powder diffraction data. A detailed understanding on

the environment of the deuteron in Scandium doped $BaSnO_3$ has been developed. Conductivity was found to peak at $x \approx 0.3$-0.4.

Experimental facilities at the ISIS neutron facility at Oxford, UK, for *in-situ* studies of fuel cell materials were demonstrated and their capability to bring about new insights on the workings of protonic conduction shown. The diffraction experiments as a function of temperature using *in-situ* impedance and *in-situ* gas flow cells gave detailed insight into the conductivity and hydration/dehydration behavior using deuterated $BaZr_{0.5}In_{0.5}O_{3-\delta}$ samples with the crystal structure remaining intact over the whole temperature interval despite expanding on deuteration and contacting on de-deuteration. The oxygen anisotropic temperature factor u_{11} was found to replicate the cell unit expansion-contraction behavior as the deuteron was inserted or removed from the crystal structure.

Keywords: proton conduction, perovskites, neutron diffraction, *in-situ* cell, Rietveld refinements, deuteron position, $BaSnO_3$, $BaZrO_3$

List of Abbreviations

TGA	Thermogravimetric analysis
XRPD	X-ray powder diffraction
NPD	neutron powder diffraction
SOFC	solid oxide fuel cells
PCFC	proton conducting fuel cells
SSS	solid state sintering
SPS	spark plasma sintering
SOL	sol-gel synthesized
EIS	Electrochemical Impedance Spectroscopy
σ	Conductivity (Scm^{-1})
Ea	activation energy
p	partial pressure of ($p(O_2)$, $p(H_2O)$)
SEM	Scanning Electron Microscopy

List of publications

This thesis is based on papers I, II and manuscript III of which I am the main author for paper II and manuscript III and coauthor of paper I. My contributions to the papers are synthesis [I, II, III], XRPD [I, II, III], NPD [II, III], EIS [I, II, III], SEM [I], rietveld analysis [III], Impedance analysis [II,] and TGA[I,].

I. Improved Proton Conductivity in Spark-Plasma Sintered Dense Ceramic $BaZr_{0.5}In_{0.5}O_{3-\delta}$. *Electrochemical and Solid-State Letters*, **13** (11) B130-B134 (**2010**)

II. *In-situ* Conductivity and Hydration Studies of Proton Conductors using Neutron Powder Diffraction. *Solid State Ionics* **2012**. *Accepted for publication*.

III. The Structure and Protonic Conduction of Scandium Doped $BaSnO_3$. *Manuscript in preparation.*

Other publications not included in thesis

I. Proton Conductivity in Mixed B-Site Doped Perovskite Oxide $BaZr_{0.5}In_{0.25}Yb_{0.25}O_{3-\delta}$.*Journal of The Electrochemical Society*, **157** (12) B1819-B1824 (**2010**)

II. The Pyrochlore to Fluorite Transition: The $Y_2(Ti_{1-x}Zr_x)_2O_7$ $(0.0 \leq x \geq 1.0)$ System. *Soon to be submitted*.

My contributions to the papers are; synthesis [I, II], XRPD [I, II], EIS [II], SEM [I], and TGA [I,]

Contents

List of Figures

The fuel cell opportunity

With a rapidly expanding world population, comes an accompanying rapid global demand for energy supply from the same limited energy sources. Hydrocarbon based energy has recently seen skyrocketing costs of fuel amid a troubled global economy. Increasingly alternative sustainable sources of energy are being investigated such as solar, geothermal, wind, biomass and hydroelectric power sources. However the setup costs, scale and geographic locations for these sources confer a disadvantage to their large scale implementation and utilization. An alternative way to tackle the energy problem is to enhance the efficiency of converting the chemical energy to electrical energy via the use of fuel cells. Proton conducting fuel cells (PCFCs) offer the capability of using hydrogen as a fuel source while operating in the intermediate temperature region of 300-500°C while offering comparable or even higher conductivity compared to solid oxide fuel cells that operate at ~700°C with greater fuel flexibility but have poor lifetimes, bulky insulation, costly high performance interconnects and longer start up times[1]. High ionic (H^{+}[2] or O^{2-}) conduction, mechanical and chemical stability are key to technological applications of fuel cells. In the intermediate temperature region, a gap[3] has been demonstrated to exist whereby materials with sufficiently high protonic do not exist. This thesis is part of the ongoing work in the scientific world to fill the gap.

1. Introduction to Fuel Cells

Fuel cells are electrochemical devices capable of converting the chemical energy in a fuel such as Hydrogen or Methane to electricity after a chemical reaction with an oxidizing agent. Through this direct conversion of chemical energy to electrical energy without any thermo-mechanical step (no kinetic energy step), fuel cells are able to achieve large efficiencies in the conversion. Efficiencies of 40-60% are often achieved while efficiencies of up to 85% can be achieved for the high temperature fuel cells in combined heat and power (CHP) setups. There are various types of fuel cells classed according to the electrolyte material, temperature of operation or mode of operation[4]. Fuel cells additionally offer fewer greenhouse emissions and lower noise pollution in comparison to diesel generators. At the heart of the fuel cell lays the electrolyte; a membrane serving to allow the passage of ions while blocking gas diffusion and electron flow.

1.1 Types of Fuel Cells

A selection of current fuel cells based on the electrolyte is briefly introduced.

1.1.1 PEMs

Polymer electrolyte membrane (PEM) fuel cells have a solid polymer as the electrolyte and operate at low temperatures ~ 80°C and typically requiring platinum catalyst that splits the hydrogen. The platinum catalyst is susceptible to carbon monoxide poisoning apart from being rather expensive and in limited supply. The fuel cells are light and hence easily applied in portable applications such as electric powered vehicles.

Anode Reaction: $H_2 \rightarrow 2H^+ + 2e^-$ (over Pt Catalyst)

Cathode Reaction: $½O_2 + 2H^+ \rightarrow 2H_2O$

Overall Cell Reaction: $2H_2 + ½O_2 \rightarrow H_2O$

1.1.2 SOFCs

Solid oxide fuel cells (SOFCs) have an electrolyte based on ceramic materials (O^{2-} conducting) such as yttria-stabilized zirconia [5, 6] operating at high temperatures (~700°C). They can be deployed in a co-generation setup to achieve efficiencies of up to 80%. Their high operating temperatures enable the use of different fuel types such as methane, hydrocarbon based fuels and even CO .

Anode Reaction: $2H_2 + 2O^{2-} \rightarrow 2H_2O + 4e^-$

Cathode Reaction: $O_2 + 4e^- \rightarrow 2O^{2-}$

Overall Cell Reaction: $2H_2 + O_2 \rightarrow 2H_2O$

The schematic of the SOFC using $H_{2\,(g)}$ fuel is illustrated in figure 1. It should be noted that on the anode side, the H_2O produced would be diluting the incoming fuel feed and the exhaust gas has to be separated to recover the unspent fuel.

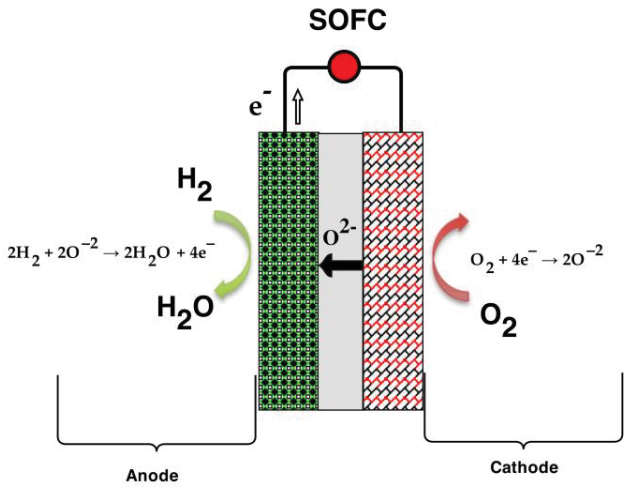

Figure 1: The schematics of a SOFC using hydrogen gas as the fuel. H_2O is produced on the Anode.

1.1.3 SAFCs

Solid acid fuel cells (SAFCs) are based on solid acids of selenates, phosphates, arsenates or sulphates of cesium that exhibit a super-ionic phase transition that is accompanied by a jump in protonic conductivity by orders of magnitude. They can operate at temperatures of ~250°C on either hydrogen or methanol [7-9]. The proton H^+ is the charge carrier.

1.1.4 MCFCs

Molten carbonate fuel cells operate at temperatures of ~ 650°C. In this case the carbonate anion (CO^{-3}) is the charge carrier. Typically $LiKCO_3$ salt in a molten state serves as the electrolyte with carbon based fuels easily being utilized. The cells are most suited for stationary applications and offer high resistance to impurities yet suffer from short life spans due to corrosion of the anode and cathode.

Anode Reaction: $CO_3^{2-} + H_2 \rightarrow H_2O + CO_2 + 2e^-$

Cathode Reaction: $CO_2 + ½O_2 + 2e^- \rightarrow CO_3^{2-}$

Overall Cell Reaction: $H_2 + ½O_2 \rightarrow H_2O$

1.1.5 PCFCs

Proton conducting fuel cells (PCFCs) are based on a ceramic electrolyte that conducts protons H^+ such as Indium-doped $BaZrO_3$ [10-12] or Yttrium-doped $BaZrO_3$ [13-17] among others. They operate in the intermediate range of 300-500°C and can be fueled by H_2 gas. The advantage of this setup compared to the SOFCs is that water does not dilute the fuel on the anode side as it is produced on the cathode as shown in figure 2. This kind of electrolyte will be the main focus of the thesis with an emphasis on synthesis, characterization and structure of $BaZr_{0.5}In_{0.5}O_{3-\delta}$. Experimental sample cell environments will also be discussed.

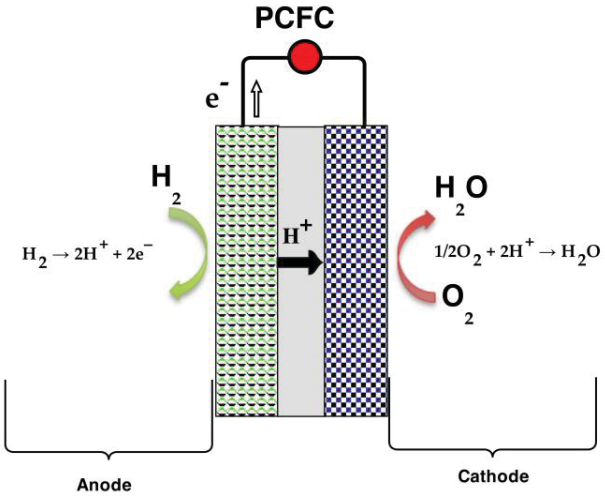

Figure 2: The schematics of a PCFC using hydrogen as a fuel and showing that H_2O is produced at the cathode.

2. Acceptor doped perovskites as Proton conductors.

The perovskite structure is unique in being so versatile in its properties (magnetism [18] catalysis [19], oxide ion conduction [20], proton conduction [17]) and applications (gas sensors, electrolytes, thermal barrier coatings and catalysts). The ideal perovskite can be described by the general formula ABO_3 that consists of corner sharing BO_6 octahedra with the A^{2+} cations aligned in cubic close packed layers with oxygen anions as shown in figure 3. Each A site cation has 12 nearest neighbour oxygen and is bigger than the B^{4+} site cation. Stability and distortion from the cubic phase is controllable by playing around with both charge and size of the A and B cations. For a smaller than ideal A site cation the BO_6 octahedra tilts to fill up space while for a larger than ideal A site cation the BO_6 shrinks to compensate.

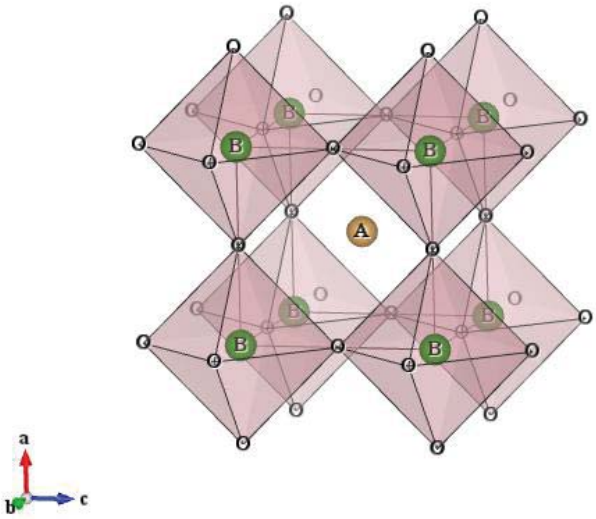

I.

Figure 3: The structure of the cubic perovskite ABO_3

A tolerance factor (*t*) serves as a rough guide in the determination of the likelihood of the formation of a perovskite at an arbitrary temperature and pressure with the ideal structure having $t = 1$.

$$t = \frac{(r_A + r_O)}{\sqrt{2}\,(r_B + r_O)} \qquad \text{Equation 1}$$

r_A =radius of A site cation

r_B =radius of B site cation

r_O =radius of Oxygen anion

This is referred to as the Goldschmidt tolerance factor and it's only a guide since other attributes size such as Jahn-Teller, lone e^- pair effects, degree of covalency and metal interactions ultimately determine the formation of perovskites. Hence the perovskite structure can be able to distort into different structures from the ideal cubic one.

Acceptor doping refers to the substitution of the B site cation with one of a lower valence state (e.g. *III*). Typical perovskites include $BaZrO_3$, $PbZrO_3$, $BaCeO_3$ [21],$LaNbO_3$ and $BaSnO_3$ [22-28] among others. The doping introduces defects that add more versatility to the perovskite structure.

2.1 Proton Incorporation and transport in perovskite.

The proton having no electron in its orbit has a small size. By itself the proton cannot occupy a defect in the material due to its small size. Defects in perovskite generally are of the intrinsic Schottky [29] type, where by both the cation and anion are missing from the ideal sites in the structure. Furthermore, one can induce vacancy formation by replacing the cations on the A or B site of the perovskite by cations of lower valence (acceptor doping) or ones of higher valence (donor doping). Acceptor doping of perovskites results in the formation of oxygen anion vacancies (defects) that are compensated by electronic holes. Generally small trivalent cations such as Yb^{3+} (0.86 Å) [29-31]

substitute for the B site while larger cations such as La^{3+} (1.03 Å) substitute on the A site [27, 29] . Hence for a perovskite of the ABO_3 type that is acceptor doped with a trivalent cation M, the Kroger-Vink notation for the reaction for the formation of oxide ion vacancies ($V_O^{\bullet\bullet}$) will be written as,

$$M + B_B^x + \tfrac{1}{2}O_O^x \rightarrow M_B' + \tfrac{1}{2}V_O^{\bullet\bullet} + B + \tfrac{1}{4}O_2 \qquad \text{Equation 2}$$

When the acceptor doped perovskites are exposed to a humid atmosphere the oxygen defects get substituted for by the hydroxyl group of which the oxygen sits on the vacant oxygen site and the proton H^+ occupies an interstitial site. This can be represented as,

$$H_2O_{(g)} + V_O^{\bullet\bullet} + O_O^x \leftrightarrow 2[OH]_O^{\bullet} \qquad \text{Equation 3}$$

Under reducing conditions *i.e.* low oxygen partial pressures, the sample loses oxygen and the following occurs,

$$O_O^x \leftrightarrow \tfrac{1}{2}O_{2(g)} + V_O^{\bullet\bullet} + 2e' \qquad \text{Equation 4}$$

Alternatively in oxidizing conditions *i.e.* high oxygen partial pressures, the following occurs resulting in the formation of electronic holes ($h^{\bullet}$),

$$\tfrac{1}{2}O_{2\,(g)} + V_O^{\bullet\bullet} \leftrightarrow O_O^x + 2h^{\bullet} \qquad \text{Equation 5}$$

Protonic conduction in acceptor doped perovskites has been demonstrated to be via the Grotthuss mechanism [32] which is a dual step process involving a reorientation step of the hydroxyl ion about its site and a proton transfer (jump) between two neighboring oxygen sites as illustrated below.

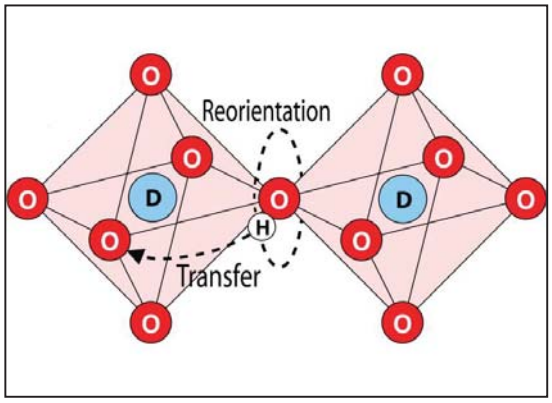

Figure 4: The Grotthuss mechanism for protonic transport in acceptor-doped perovskite. D is the dopant, O is Oxygen and H is the proton.

The product of the charge (q), mobility (μ) and concentration (C_{H+}) of protons is referred to as protonic conductivity (σ_{H+}), equation 6, which can alternatively be expressed as the diffusivity effectively introducing the importance of temperature equation 7 where T is the absolute temperature and k_B is Boltzmann's constant. The temperature dependence results in an Arrhenius behavior if the proton concentration C_{H+} is held constant equation 8.

$$\sigma_{H^+} = q.\mu_{H^+}.C_{H^+} \qquad \text{Equation 6}$$

$$\sigma_{H^+} = \frac{(q.D)}{(k_B.T)} \qquad \text{Equation 7}$$

$$\sigma = A.e^{(-E_a/RT)} \qquad \text{Equation 8}$$

Where A is a pre-exponential term containing many factors among them the number of mobile species, charge of the species, the number of directions for the jump event, the frequency of the jumps and the volume. E_a is the activation energy required to be overcome for the conduction process to occur and R is the molar gas constant. Given that the frequency of the jump in proton conductors concerns the O---H bond stretching vibrations, it clear that substitution for a heavier isotope in this case deuterium D^+, would result in slower vibrations of the bond and hence yield a smaller jump frequency. Consequently the conductivity of the heavier deuterium isotope (atomic

mass = 2.014 u) would always be discernibly lower than for the lighter isotope, the proton (atomic mass = 1.007u). This phenomenon is used as a quick test to verify that indeed protonic conduction is present in a sample. It is referred to as the isotope effect.

2.1.1 Materials requirement for the electrolyte

As a requirement for a good protonic-based electrolyte the material should be impermeable to gas, be highly densified, block electron conduction and possess protonic conduction ($\sigma = 10^{-2}$ Scm^{-1} for practical use). One of the challenges is that some materials are not easily sinterable and therefore possess a lot of grain boundaries which reduces the total conductivity. To overcome this, sintering additives[13], wet-chemical [11] /SOL [33], and SPS [34] are used to improve densification at lower temperatures hence reducing the number of grain boundaries present. This often results in higher conductivity.

3. Experimental techniques

3.1 Sample preparation

3.1.1 Solid State Sintering

Synthesis of perovskite materials is performed via the solid-state sintering route in which stoichiometric quantities of the metal carbonates and oxides, which have been heated to remove moisture before weighing, are mixed in an agate mortar and hand milled with a pestle in the presence of ethanol (99.5%). The dried powder is then

1. Calcinated at 1000°C for *t* hours to decompose the carbonates.
2. Pressed into pellets and heated to a higher temperature for *t* hours.
3. The pellet is crushed and milled, the resulting powder is checked for purity via X-ray powder diffraction and if not pure step 2 and 3 were repeated until the sample is found to be pure.

Occasionally ball milling with a Planetary ball milling equipment can be used in the intermediate stages between the heating steps especially when large sample amounts (>5g) are required in a series. The milling balls and the milling house can be made of alumina, zirconia or steel. A typical milling run has the following parameters; 500 rpm, 20 minutes of milling, 5 minutes of cooling and 40 repetitions.

3.1.2 Spark Plasma Sintering (SPS).

In this technique, the sample is made dense by holding it under pressure in a graphite die under vacuum while passing a pulsed DC current through it. Pure sample powders are ball milled into fine powders and put in a graphite pressure die and mounted onto a Dr. Sinter 2050 (Syntex Inc., Japan) SPS setup. The die chamber is evacuated to 6 Pa and a pulsed DC current is applied through the die. This rapidly heats the sample under pressure (100°C/min) with a final sintering temperature at 1250°C. The sample is held at that temperature for 5 min at 100MPa then cooled after switching off

the current and releasing the pressure. The sample cools down to room temperature within 10 minutes. The SPS sample is then slightly polished and oxidized at 700°C for some time to remove traces of carbon (from the die) on the surface. The samples have a density of ~90% of the theoretical value.

3.1.3 Hydration.

The hydration is carried out at 300°C under N_2 gas flow saturated with water vapor at 76.2°C (~0.42 atm, $p(H_2O)$) for several days for powdered and pellet forms of the materials. Pellet samples for *in-situ* neutron diffraction combined with electrochemical impedance spectroscopy are deuterated hydrothermally by inserting them in a Teflon lined autoclave with a precise amount of D_2O equivalent to the amount of oxygen vacancies present in the sample at 210°C for 12 hours. This can be done for powdered samples too. Thermo-gravimetric analysis (TGA) of the hydrated powder samples was carried out in a stream of N_2 gas by heating to > 800°C at a given rate in a NETZSCH STA 409 PC™ instrument to determine any mass losses that occur and their associated temperatures.

3.1.4 Pellets for conductivity.

Pellets for conductivity were painted with platinum ink and the organics burnt off at 800°C. Impedance of the samples was measured at 1 V rms while sweeping the frequency from 1 MHz to 1Hz. A Solartron™ 1260 frequency response analyzer connected either to a Probostat conductivity cell (paper 1 and 3) or an *in-situ* conductivity cell [35] (paper2) was used to collect electrochemical impedance data.

3.2 Characterization techniques.

3.2.1 Powder Diffraction.

The primary characterization of the samples purity, crystal structure and reaction progress in this study was performed via the powder X-ray diffraction technique. Through irradiating a sample

with radiation of wavelength comparable to its atomic spacing's, constructive and destructive interference will occur between the lattice planes in the crystal, resulting in a diffraction pattern. This pattern presents a detailed picture of the inner structure describable in terms of the symmetry of the unit cell and its dimensions, fractional coordinates as well as the chirality. For an X-ray pure material, all its peaks in the diffractogram could be indexed and assigned a space group. Hence this technique is able to "fingerprint" material's since the materials X-ray pattern is dependent on the atomic number, position of the atoms, and the type of unit cell as well as its size. Therefore despite two or more materials having the same space group, their diffractograms will be essentially unique.

Crystalline materials are characterized by the orderly periodic arrangement of atoms and possess lattice planes (visible from single crystal diffraction data) described by integer values *h, k, l* known as Miller indices when they are parallel, in which case then the distance between two of these planes is denoted d_{hkl}. In reciprocal space however the distance between reciprocal space planes is ascribed $1/d_{hkl}$. Given a monochromatic X-ray beam and a set of parallel planes in the crystal, constructive interference will occur if the Bragg conditions are fulfilled. These conditions are: the path length between two waves constructively interfering is a multiple integer (n) of the wavelength and the wavelength (λ) is comparable to inter-atomic distances (inter-lattice distances). The constructive interference will result in peaks appearing in the collected diffraction pattern plotted as the intensity as a function of 2θ. This is articulated in the Bragg equation below.

$$2\mathrm{d}_{hkl}\sin\theta_{hkl} = n.\lambda \qquad \text{Equation 9.}$$

For a material like $BaZr_{0.5}In_{0.5}O_{3-\delta}$ that is cubic in nature, then the cell parameter "*a*" can be calculated as below,

$$\frac{1}{d^2} = \left(\frac{h^2+k^2+l^2}{a^2}\right) \qquad \text{Equation 10.}$$

where *h,k,l* are the Miller indices , d is the interplanar spacing (figure 5) . The Bragg equation is illustrated below whereby P1 and P2 are the planes, X and Y are the incident beams, Y* and X* are the diffracted beams, d is the interplanar distance and θ is the incident angle to the plane. The path difference between the beams, ABC, is hence equivalent to 2dsinθ**.** To pinpoint the expected peak positions the two equations (9 and 10) can be combined to yield,

$$\left(\frac{\lambda}{2a}\right)^2 = \frac{\sin^2\theta}{h^2+k^2+l^2} \qquad \text{Equation 11}$$

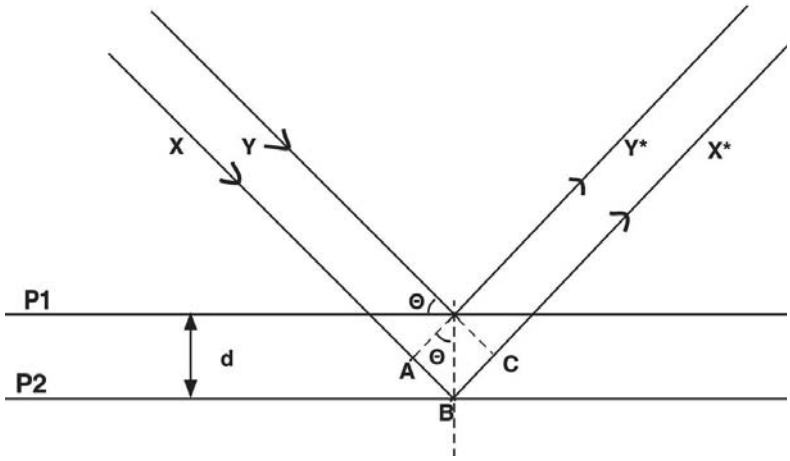

Figure 5: An illustration of the Braggs law showing that the path length difference travelled by the second X-ray beam X, ABC can be calculated using 2dSinθ where d is the interplanar distance, θ is the incident angle, P is the plane and X and X' are the incident and diffracted beams respectively.

Whilst varying the Bragg angle (θ), the above equation can be satisfied for a number of d-spacings in the polycrystalline material. The detector samples intensities over a 2 θ angular range, which itself is the angle between the diffracted beam and the incident beam. The powder diffraction analysis utilizes peak profile, intensity position and width of peaks to unmask the crystal structure of the samples being studied. The relative concentration of different phases in the sample, the atomic arrangement in the different phases and the identity of those phases can hence be obtained.

The X-ray equipment used in this project was the Brüker D8 Advance™ diffractometer with a monochromatic Cu kα radiation with a wavelength of 1.5406 Å. A database (ICDD: International Centre for Diffraction Data) was used to identify the phases in the sample.

Neutron powder diffraction (NPD) was performed at the POLARIS [36] beam line at the ISIS large scale facility, a spallation source. Neutrons for diffraction studies are normally generated from nuclear reactors or spallation sources. In a reactor source the neutrons produced as a result of fission processes while in spallation source the neutrons are produced by targeting high-energy protons on a suitable metal target. In the former source the neutrons are produced continuously while pulses of neutrons are produced from spallation source.

The advantage of using NPD is that the scattering power of the atoms is not dependent on the number of electrons hence both light atoms such as hydrogen, can be identified in the presence of heavier atoms unlike in X-ray powder diffraction (XRPD). A good application of this ability is the determination of Hydrogen position in metallic hydrides such as europium hydride [37], a hydrogen storage candidate. Additionally the precise atomic positions in a unit cell are best-refined using neutron data. Oxide superconductors require the precise location of the atoms to be located and also the site occupancy to be finely refined so as to elucidate the source of superconductivity [38, 39].

The Energy dispersive principle of neutron diffraction, commonly known as time of flight (TOF) is applied in pulsed neutron sources, which deliver white band neutrons (neutrons with varying speeds) on to the sample. Given a neutron travel path, the fast (shorter λ) neutrons would separate from the slow (longer λ) ones in the incident beam. All of these wavelengths (λ's) hit the sample can, made of neutron transparent material (Vanadium), before being diffracted by the contained sample onto the detectors.

The scattered beams λ is obtained by measuring the total time of flight (t) from the source to the sample and then to the detector given that the total flight path length (L) is available. Hence, t can be related to λ via the following equation [40],

$$t_{\mu sec} = 252.78 * L(m) * \lambda(\text{Å}) \qquad \text{Equation 12}$$

with values plugged in at indicated units. Therefore, for a wavelength (λ) of 3 Å and a path length (L) of 20 meters the TOF would be 15.16 ms. In practice it is important to achieve good resolution of the Bragg peaks by having a long flight path. This introduces a frame overlap problem that occurs due to faster neutrons overtaking slower neutrons to the detectors hence contaminating the collected data. The set of neutron λ's free of overlapping (Δλ) are obtained by considering that [40]:

$$t_{max} - t_{min} = \Delta t = \frac{1}{\nu} \qquad \text{Equation 13}$$

where ν is the pulse frequency of the source and hence Δλ is

$$\Delta\lambda(\text{Å}) = {}^{3956}/_{L(m) * \nu(Hz)} \qquad \text{Equation 14}$$

The frame overlap can be removed by inserting waveband choppers between the source and the sample to exclude a number of incident beam pulses so that instead of collecting the data in a number of wavelength sections, each Δλ in value, the entire diffraction pattern can be collected at one particular setting (a specific pulse of each cycle, ν).

For the POLARIS [36] powder diffractometer at the ISIS facility in Oxford, UK, the sample position is 12m from the source hence the available maximum wavelength is 6.59 Å, using equation 14 (above). There are three sets of detector banks, the low angle, the 90° and the backscattering banks each covering 14°-27°, 86°-94° and 130°-155° 2 θ range respectively.

3.2.1.1 Rietveld Analysis

The Rietveld method[41, 42] is a least squares refinement that fits a theoretical model to experimental data. By altering different parameters such as; *zero point (detector), lattice parameters,*

background noise, temperature factors and position of the atoms, the difference between the theoretical model and the experimental data can be minimized. However, it is important to remember that convergence of the least-squares calculation between the model and experimental patterns provides no guarantee that the model is physically meaningful. The convergence of least-square calculation may occur due to false minima. Therefore, a good chemical knowledge is essential.

An important aspect with the Rietveld method is that the user is in control of the information given through the refinement and can hence be able to re-modify the parameters as needed. This can be done by, for example, comparing the bond lengths from the Rietveld refinement with known bond lengths from literature hence avoiding unreasonable bond lengths in the refinement.

This data is then fitted into the Rietveld Analysis software such as GSAS [43] where the theoretical model is refined by altering different factors with a visual inspection of the graphical output. CelRef software in this study was used to extract the initial cell parameters, which were used in the Rietveld analysis.

3.2.2 Thermogravimetric analysis (TGA)

TGA is an experimental method in which the mass change of a sample is measured as a function of temperature or time. The mass change indicates whether the sample undergoes decomposition or absorption/desorption when heated or cooled under controlled atmospheres. In the case of decomposition it's also possible to calculate which types of molecules are lost in the process given a bit of chemical knowledge of the sample. The mass change is this case an inherent property of the material and can be quantitatively linked to physical or chemical processes occurring in the sample.

In the case of proton conductors, during the hydration process, protons are incorporated into the structure of the material, which results in an increase in mass of the sample. Similarly, for pre-

hydrated samples a mass loss is observed upon heating under a dry inert atmosphere. By following the mass change of the samples quantitatively, it is possible to know the amount of protonic defects formed during the hydration process.

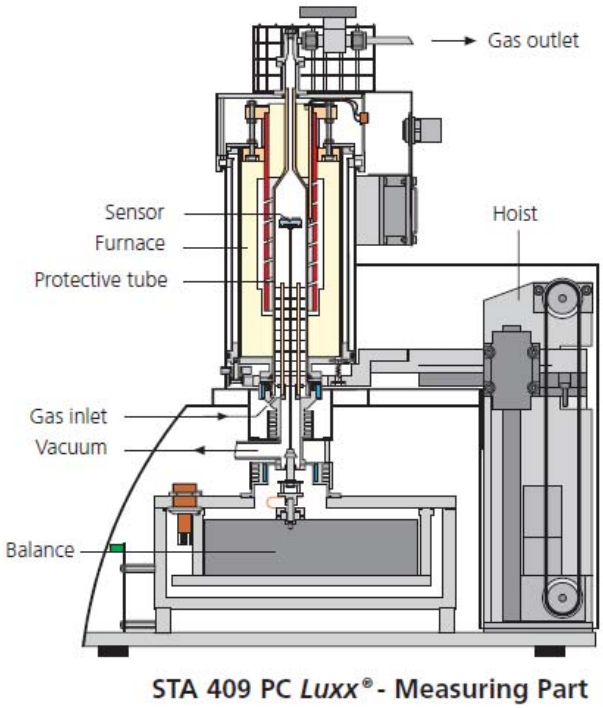

Figure 6: The schematics of a NETZSCH STA 409 PC instrument used for the TGA measurements.

The instrument used for TGA the investigation is a NETZSCH STA 409 PC (Figure 6) with alumina crucibles and Nitrogen gas as the supporting gas. The reference container is run empty, and a correction run is always run before performing a new series of investigations.

Before every run the furnace outlet top valve is shut, then the vacuum pump is turned on and the chamber evacuated and refilled twice with nitrogen gas using the back valve for evacuation and

the side valve for refilling with inert gas e.g. N_2 or Ar (to at least 1mbar). After the second refill, the vacuum and refill valves are shut and the pump is turned off. Before a run the initial conditions are turned on and the top valve outlet is opened. In general, 15 minutes time is elapsed before the measurement is started in order to ensure the gas flow equilibration with the set flow rate.

3.2.3 Electrochemical Impedance Spectroscopy (EIS)

The method measures the electrical impedance that is frequency dependent only. In most cases a ceramic materials electrical properties are composed of various processes such as diffusion and components such as grains and grain boundaries. When investigating a material, special interest is paid to separate the components, grain, grain boundary, electrode processes and diffusion contributions to the electric properties of the material. Ionic conduction, defects and electric conduction can be characterized as well as ferroelectric and dielectric properties of a material.

Typically a complex plane plot where the imaginary impedance (Z") is plotted against the real impedance (Z') is used to present the results of an experiment. The data is composed of semicircles, each of which can be ascribed to the circuit elements the resistor (R) and a constant phase element (CPE), an imperfect capacitor, in parallel. For an ideal polycrystalline material, the bulk behavior (G) is found at the high frequency region (to the left of a complex plane plot), the grain boundary (GB) in the middle frequencies and the electrode behavior (E) in the low frequency region (to the right) as shown in the figure below. This is due to the fact that grain boundaries generally have resistances higher than those of the grain bulk hence it is advantageous to minimize the amount of grain boundaries by having larger grains in the sample.

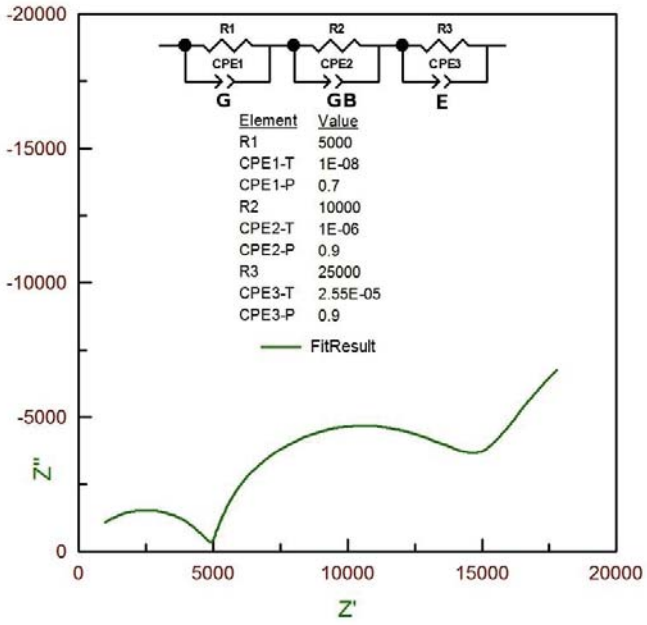

Figure 7: A simulated plot in the complex plane showing three semi-circles in the frequency range scan of interest. From the left, each semi-circle represents the grain bulk, grain boundary and the electrode responses. The insert shows the respective circuit models used for the plot.

The resistances of each of the components in a material are indicated by the distance across the semicircle along Z'. In practice the results are fitted with circuit models from which the resistances (R (Ω)) are obtained. Impedance accounts for capacitance and inductance effects, which vary with the frequency (*f*) of the current through the sample. Hence impedance is not equivalent to resistance unless the circuit has no capacitors or inductors present. Impedance (Z) is made up of two parts, the resistance R (independent of *f*) and the reactance X (dependent on *f* due to capacitance and inductance). A phase shift between current and voltage is caused by capacitance and/or inductance implying that R and X have to be summed up as vectors at right angles to each other to give (Z), see figure 8 where X_L is the inductance component and X_C is the capacitance component of reactance X.

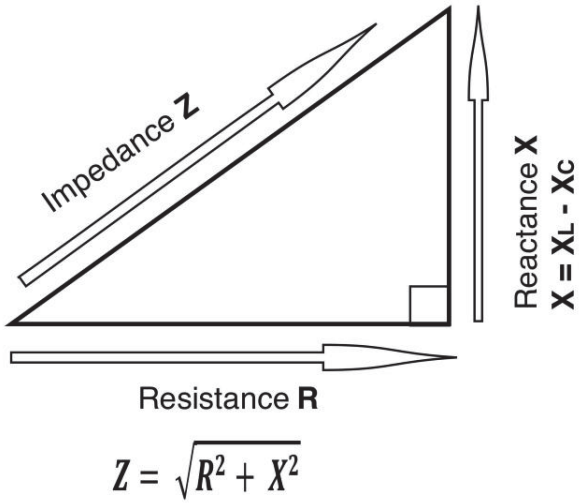

Figure 8: Illustration of the vector addition of resistance and reactance to give the impedance.

The relation between Z' and Z'' as used in the complex plane plot is:

$$\left[Z' - {}^{R}/_{2}\right]^2 + (Z'' - 0)^2 = \left[{}^{R}/_{2}\right]^2 \qquad \text{Equation 15}$$

It should be noted that it's not always possible to observe three semicircles representing the three components of the polycrystalline sample, as some may not be expressed in the frequency range selected for the experiment. The capacitances of the associated resistances are used to classify the resistances as grain bulk resistance (10^{-12} F), grain boundary resistance (10^{-11}-10^{-8} F), sample-electrode-interface resistance (10^{-7}-10^{-5} F) and electrochemical reactions (10^{-4} F).

The conductivity (σ) of a sample is often plotted by, taking its logarithmic value as a function of 1/T. The values are always normalized for the samples dimensions by (equation 16)

$$\sigma\ (Scm^{-1}) = \frac{T(cm)}{R(\Omega) * A(cm^2)} \qquad \text{Equation 16}$$

3.3 In-situ Characterization Techniques

These are defined by their ability to observe the phenomenon of interest as it occurs and in real life conditions as much as possible. Typically they comprise of a specially built sample environment cell that is mounted in a setup that facilitates the characterization of the sample under a given set of conditions while observing the phenomena using one or more experimental techniques. In case of two probing methods, the data sets are in-sync in terms of the timescale.

In this thesis, *in-situ* impedance measurements as a function of temperature are performed while collecting neutron diffraction data, additionally the hydration or dehydration behavior using D_2O as a function of temperature is investigated using neutron diffraction in a setup that can also monitor the partial pressure of oxygen $p(O_2)$ when oxide ion conductors are being investigated. The obvious advantage of this is that all the data collected will be from just one sample and not different batches or pellets of the sample, so effects attributable to microstructure for example are the same over all the experiments and the sample conditions are identical. The two separate setups designed for use at the ISIS beam lines are discussed below.

3.3.1 *In-Situ* Humidification Setup

This consists of the gas flow cell [44] coupled to a gas humidification system which is itself connected to a gas mixing system as illustrated in figure 9 below. The gas mixing system makes use of mass flow meters and precise pressure regulators that allow for simultaneous precision mixing of four gasses, currently O_2, Ar, CO_2, and CO. This allows for the precise setting of the oxygen partial pressure, $p(O_2)$, of the inlet gas. The *in-situ* gas flow cell consists of an oxygen sensor (3), which is positioned directly above the sample (10), usually in the form of porous pellets that are stacked on the quartz frit (11), and below is a thermocouple (12). The gas feed (13) is at the bottom of the quartz cell and the outlet at the top (1). The inlet is connected to the H_2O/D_2O injector (7) and gas mixing system (8). The furnace setup surrounds the narrower bottom part of the cell and consists of an electrical

heating element (15) surrounded by three heat shields (14) all of which are made of thin vanadium sheets.

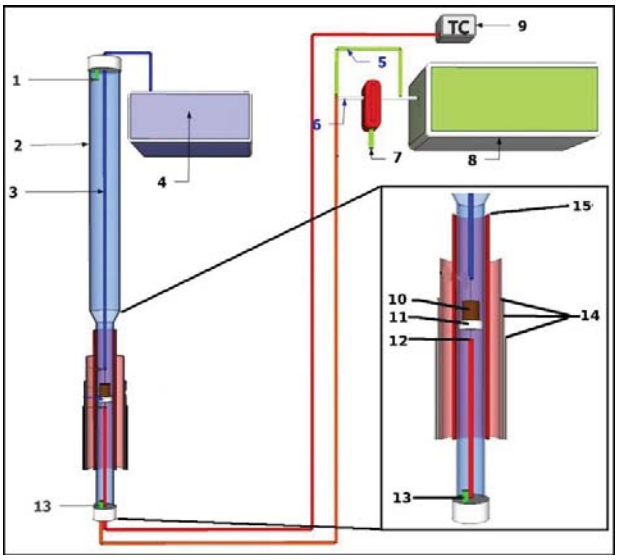

Figure 9: The high temperature *in-situ* humidification cell setup. The components are named in Table 1.

The gas humidification system (7) consists of a thermally insulated gas-washing bottle partially filled with D_2O and covered with a heating cord so that the contents can be kept at a constant set temperature. Through ball valves, the liquid content can be refilled by, blocking the gas inlet/outlet and opening alternate liquid input/output injection via a syringe. This provides the wet gas (6) to the *in-situ* cells. A thermocouple inside the bottle linked to a temperature controller sets the required temperature of the contents. A valve before the bottle allows dry gas to bypass the setup completely making it easy to switch between a humid and a dry gas flow (5).

3.3.2 *In-Situ* Impedance Spectroscopy Setup

The *in-situ* impedance spectroscopy cell [35], see figure 10, consists of Pt electrodes (12) positioned in a recessed cavity inside two boron nitride (BN) shields (8,10), with platinum mesh added to ensure good contact. These elecrodes are springloaded and the electrical leads are also

shielded by BN (14). The sample pellet (9) is positioned between two BN shields (8,10) such that diffration occurs only from the sample and not the hidden electrodes. A thermocouple (4) connected to a temperature controller (17) sits embeded within the bulk of the upper BN sample shield (8) in which the Pt electrical leads are embeded.

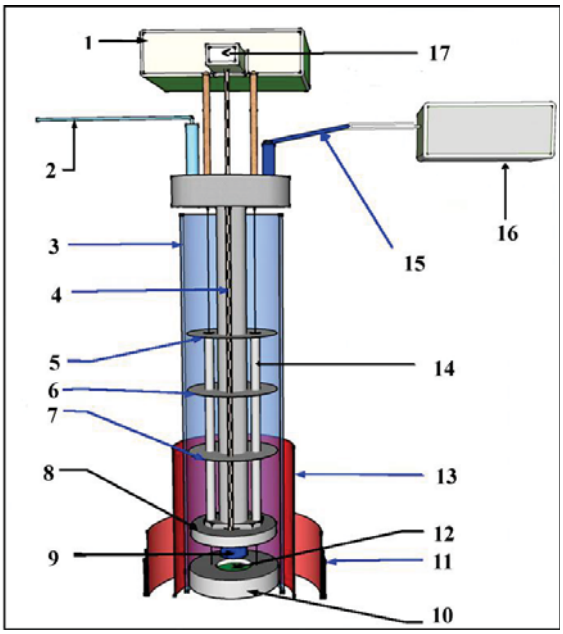

Figure 10: Schematics of the *in-situ* impedance spectroscopy cell. The components are named in table 2.

The furnace consists of an inner electrical heating element (13) and three outer heat shields (11) all made of thin vanadium sheets at the center of which lies the quartz tube (3) bearing the mounted sample assembly. There is a gas inlet (15) and outlet (2) which can be used to supply and evacuate the cell as required. A Solartron S-1260 frequency response analyzer (1) is coupled to the cells Pt leads and is used to collect impedance data. The gas inlet is connected to the gas mixing system (16). A series of tight fitting heat radiation baffles (5 - 7) ring the central support column. The sample is mounted and tightly held between the BN shields with the electrodes (faces) hidden from the neutrons but the side exposed to neutrons. The whole setup is then inserted into the neutron beam line.

4. Results and Discussion

4.1 Improved proton conductivity in spark-plasma sintered dense ceramic $BaZr_{0.5}In_{0.5}O_{3-\delta}$

$BaZr_{0.5}In_{0.5}O_{3-\delta}$ was synthesized first via the solid-state synthesis (SSS) method from $BaCO_3$, In_2O_3 and ZrO_2 with the latter two having been pre-dried overnight at 800°C. The heating stages were; 1000°C for 8 h, 1200°C for 72 h and 1350°C for 48 h with intermediate grinding and pressing of tablets in a 13 mm die. One pellet for conductivity was kept aside.

The final pellets being pure were ball milled into fine powders in an alumina milling house, dried and then processed via spark plasma sintering (SPS), at a final temperature of 1250°C, to achieve high densities of the pellets for conductivity.

Powder X-ray diffraction showed the existence of a single phase in the SSS sample while the SPS processed sample had trace impurity peaks that disappeared once the sample was heated to 1500°C in air. The main phase was indexed as cubic $Pm\bar{3}m$. The impurity in the SPS sample was from the graphite die used, which served as a source of carbon that reacted with the sample on heating at 700°C to remove the graphite. This resulted in the formation of $BaCO_3$, hence segregation of the ZrO_2 and In_2O_3 due to barium deficiency. However, when the sample was heated to 1500°C, the three components reacted to yield a single phase of the desired material hence no impurities. The same behavior has been reported for $BaY_xZr_{1-x}O_{3-x/2}$ by Anselmi-Tamburini *et al*.[45]

TGA results of pre-hydrated SPS sample showed the existence of a mass loss beginning at 300°C as expected [10, 46] for this proton conductor. This confirmed that protons were present in the sample. However there was still a mass loss in the isothermal step at 900°C which is attributable to the loss of carbon based species given SPS processing was in a graphite die.

Micro-structural properties investigated by (SEM) indicated that SSS samples had bigger grain sizes compared to SPS samples given that the soaking time at high temperature was very short ≈

5 min versus 48 hours for SSS samples. The grain size was in the order SSS > SPS > SOL (sol-gel synthesis ref [47]). Neither specific grain boundary orientation nor secondary phases were observed using SEM.

Conductivity wise, wet hydrogen atmosphere exhibited the highest bulk and total protonic conductivity in the region of 150-600°C compared to wet argon and dry Ar atmospheres for the SPS sample. The bulk and total conductivities for wet argon runs were slightly higher than those of prehydrated sample on heating under dry Ar, see figure 11b. The bulk conductivities could only be distinguished from the grain boundary conductivities in the range of 150-300°C, see figure 11a.

The activation energies (150–350°C, figure 11b) of total conductivity for the as-prepared samples (under different humid atmospheres on cooling) and for the heating cycle of pre-hydrated (pre-hyd.) sample (under dried Ar atmosphere) were in the range of 0.39–0.62 eV and consistent with typical protonic conduction activation energies, 0.4-0.5 eV, of the best proton conductors, Y-doped $BaZrO_3$ or $BaCeO_3$ [2, 48]

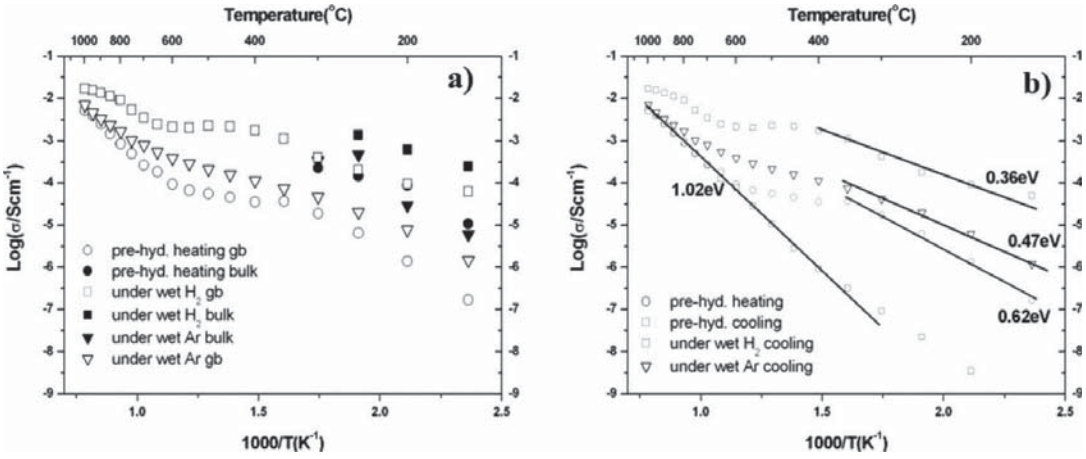

Figure 11: Conductivity of SPS $BaZr_{0.5}In_{0.5}O_{3-\partial}$ sample under different atmospheres (a): bulk and grain boundary (gb) and (b): total.

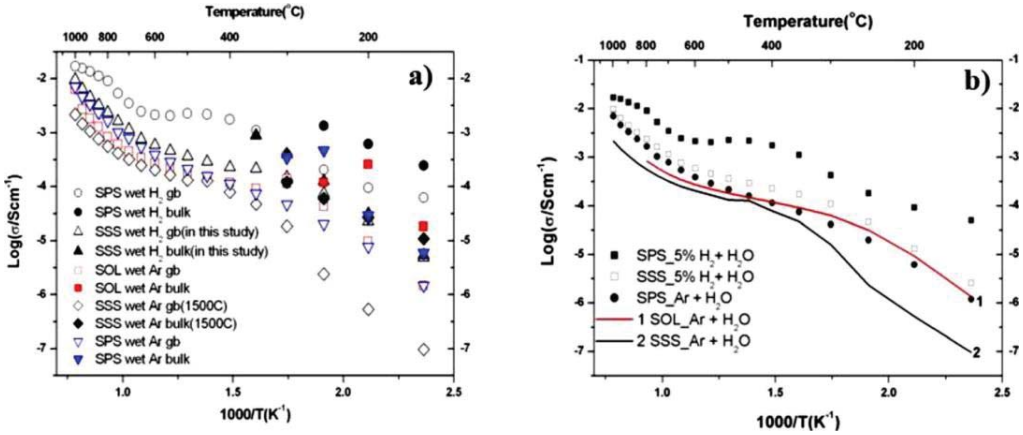

Figure 12: Comparison of (a) bulk and grain-boundary (gb) NB: SSS sample prepared in this paper is included (b) total conductivity under humid atmospheres. Data for SSS (1500°C), SOL, and 1–2 have been taken from Ref[47]

For comparison data from SSS (1500°C) [47] samples and sol gel synthesis (SOL 1100°C) [47] was plotted together with SPS conductivity data showing that both bulk and total conductivity values for SPS sample in wet hydrogen were the highest. Protonic conductivity of SPS and SOL samples in Wet Ar were almost the same while those of SSS were an order of magnitude lower between 150-250°C, (SPS ≈ SOL > SSS) see figure 12b.

Under dry argon atmosphere for prehydrated samples, on heating the effect of the microstructure on conductivity was exposed. Conductivity in Dry Ar heating followed the following trend SSS > SPS > SOL .This replicated grain size behavior.

On the cooling cycle, where all protons have been driven out of the samples on heating (E_a= 085[47]-1.02 eV), all the conductivity values are similar as expected since there is no protonic conductivity in the dry atmosphere, see figure 11b. The characteristic plateau at 300°C-650°C matches with the mass loss behavior for the TGA analysis confirming that protons are the source of conduction in the 150°C-650°C under wet atmospheric conditions.

Platinum wire and paste used for the electrodes is a well-known reduction catalyst and has been shown to be capable of catalytically reducing lattice oxygen($V_O^{\bullet\bullet}$) in the presence of H_2. In wet $H_{2,}$, H_2O species would react about the triple phase boundary with Pt resulting in higher surface coverage of $OH_O^{\bullet}$ [49] .This would enhance the charge transfer conductivity resulting in higher total conductivity.

Given that the grain sizes were in the order SSS > SPS > SOL one would expect that conductivity would be highest for the SSS sample with the least number of grain boundaries. Hence there seems to be a conflict in the conductivity results given that under dry Ar conductivity is in the order, SSS > SPS > SOL (expected) while in wet Ar it is in the order SPS ≈ SOL > SSS (unexpected). This discrepancy can be explained by considering that the surface of the SPS and SOL samples has higher surface area hence faster reaction kinetics for equation 3 below,

$$H_2O_{(g)} + V_O^{\bullet\bullet} + O_O^x \leftrightarrow 2[OH]_O^{\bullet}$$

Interestingly grain boundary conductivity under wet H_2 for SPS sample is higher compared to SSS sample despite the smaller grain sizes, this needs further investigation.

4.2 In-Situ Conductivity and Hydration Studies of Proton Conductors using Neutron Powder Diffraction

Synthesis of $BaZr_{0.5}In_{0.5}O_{2.75}$ powders was performed mixing stoichiometric amounts of $BaCO_3$, ZrO_2, and In_2O_3 and processing via solid state synthesis. The heating stages were; 1273 K for 8 h, 1473 K for 72 h and 1623K for 48 h with intermediate grinding and pressing of tablets in a 13 mm die. Two sets of 10 mm pellets were fabricated using finely milled powder and pressing under 8 tons of pressure for dense pellets and 4 tons of pressure for more porous pellets. The dense pellets were used for *in-situ* impedance spectroscopy measurement (with painted Pt electrodes) while the porous pellets were used in the *in-situ* humidity experiment. All pellets were sintered at 1723 K for a period of 24 hours. The dense pellet, painted fully with Pt ink on both faces was heated at 1273 K to burn off the organics. The pellets were then put in a Teflon lined hydrothermal bomb and D_2O added before hydrothermal deuteration in a furnace pre-set at 483 K for 12 hours.

The experiments were carried out at the ISIS facility using the Polaris neutron powder diffraction instrument [36].Analysis of the diffraction data used the GSAS [43] software and the accepted structural model for $BaZr_{0.5}In_{0.5}O_{2.75}$ as a cubic perovskite with space group $Pm\bar{3}m$ [10].Two types of *in-situ* cells were used for the experiments:

- *In-Situ* Humidification Experiment: Using a custom high temperature gas flow cell [44] coupled to a temperature controlled gas humidification charged with deuterium oxide (D_2O).
- *In-Situ* Impedance Spectroscopy Experiment: Using a custom made resistance cell [35] coupled to a Solartron™ 1260 frequency response analyser .

4.2.1 *In-Situ* Humidification Experiment

In-situ neutron diffraction of the porous samples was made using the high temperature gas flow cell with the H_2O/D_2O injector connected. The porous pellets were stacked on the quartz fritz up

to a height of ~4 cm. Data was collected on the as prepared sample in steps of 50 K in the following sequence:

A dry sample was loaded into the cell and heated quickly to 1100 K in a dry atmosphere without any data collected.

I. Cool down to 373 K in a dry atmosphere, with data collection –○ symbols.
II. Ramp up to 1073 K in a wet atmosphere without any data collected.
III. Cool down to 373 K in a wet atmosphere, with data collection –Δ ▲ symbols.
IV. Ramp up to 1073 K in a dry atmosphere with data collection –∇ ▼ symbols.

The lattice parameter data collected for measurements during procedure I, III, and IV of the sample cell testing has been plotted in figure 13. Data for procedure I indicates a single phase (○) whose lattice parameter increases linearly with temperature under dry Ar. Procedures III (Δ ▲) and IV (∇ ▼) data indicate the presence of two phases, a deuterated phase (filled symbols) and a non-deuterated phase (open symbols).

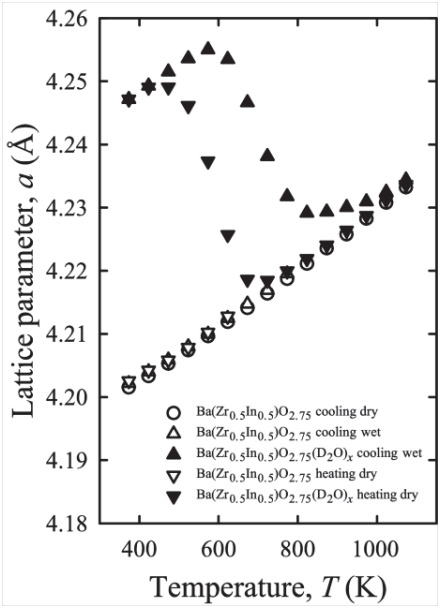

Figure 13: Variation of the lattice parameter as a function of temperature while the sample was exposed to dry or wet argon atmosphere. Two distinct phases are present when deuterons are present in the sample.

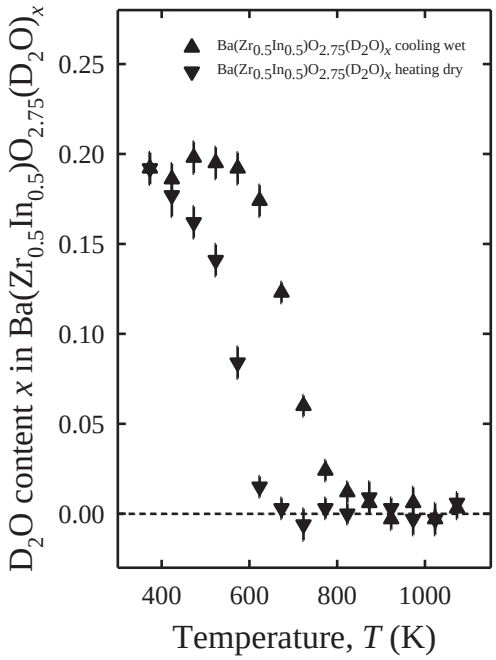

Figure 14: Variation of the refined D_2O content as a function of temperature under dry Ar heating and under wet Ar on cooling.

This implies that the sample is only partially deuterated. Figure 14 shows the refined deuterium fraction x in $BaZr_{0.5}In_{0.5}O_{2.75}(D_2O)_x$ as a function of temperature for procedures III and IV in those cases where a significant deuteron concentration is present in the sample. A maximum of 80% (x~0.20) deuteration is achieved under wet Ar conditions at 500 K. Interestingly, under wet Ar atmosphere the temperature for maximum deuteration (max. x) or mobility (T at which deuterons start leaving) is higher by 200 K as compared to dry Ar conditions. This shift is brought about by the D_2O present in the gas stream, which shifts the reaction (Equation 3) to the right despite the high temperature favoring the reaction to proceed towards releasing humidity from the sample.

$$H_2O(g) + V_O^{\bullet\bullet} + O_O^x \leftrightarrow 2OH_O^{\bullet} \qquad \text{Equation 3}$$

The shift is confirmed to be due to deuterons in the system by a plot of the D_2O fraction in the system, figure 14, which replicates the shift behavior in the lattice parameter (figure 13).

The model used for the refinement composed of two phases $BaZr_{0.5}In_{0.5}O_{2.75}$ (un-deuterated) and $BaZr_{0.5}In_{0.5}O_{2.75}.(D_2O)_x$ (deuterated). The weight fractions obtained from rietveld refinements for procedure IV at 373K were 11.7% and 88.3% respectively. The D^+ were modeled in the 12*h* sites at (1/2, y, 0) with the y parameter fixed at the value of 0.217 according to the paper by Ahmed *et al.*[50]

The oxygen thermal parameters were modelled anisotropically and indicated an approximately linear behaviour with increasing temperature for the u_{22} (and identical u_{33}) for both deuterated and non-deuterated cases (figure 15). However, the u_{11} behaviour when deuterons were present in the structure followed the lattice parameter behaviour observed in parts III and IV of the experimental procedure, see figure 15.

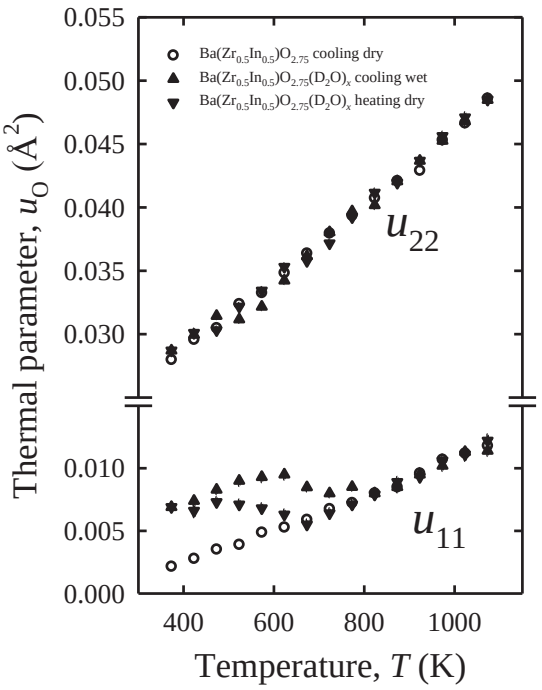

Figure 15: Variation of the oxygen thermal parameter as a function of temperature.

This would indicate that only thermal vibration/static disorder in the u_{11} direction are associated with the migration of the proton and hence the conductivity. Further work is planned on investigating this phenomenon in detail with additional perovskite systems.

4.2.2 *In-Situ* Impedance Spectroscopy experiment

The *in-situ* impedance spectroscopy experiment involved clamping the dense pre-deuterated pellet in the boron nitride shielding such that the painted electrodes were buried within the recess on the boron nitride and make contact with the spring loaded Pt electrodes. This resulted in a neutron line of sight in which the neutron beam only hit the side of the exposed bulk sample. Continuous impedance measurements were made on the pre-deuterated sample in dry Ar gas for a heating and cooling cycle (373 K - 973 K) with a neutron powder diffraction data collection every 50 K. The measured frequency range was 1 Hz - 1 MHz with a sine wave of 1 V rms.

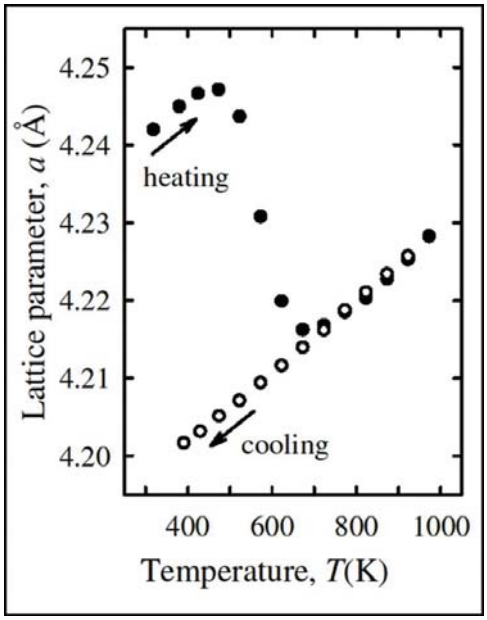

Figure 16: Variation of the lattice parameter, *a*, of a pre-deuterated $BaZr_{0.5}In_{0.5}O_{2.75}$ sample as a function of temperature under dry Ar gas.

The lattice parameter plotted as a function of temperature showed that between 500 and 800 K the deuteron leaves the structure completely (figure 16). Only one phase was present on heating, indicating that deuteration of the sample was complete. Between 800 and 1000 K the lattice

parameter for heating and cooling match, indicating the absence of deuterons in the structure. During heating up to 750 K, the cell parameter is larger than on cooling (T ≤ 750 K), due to the incorporation of deuterium into the structure.

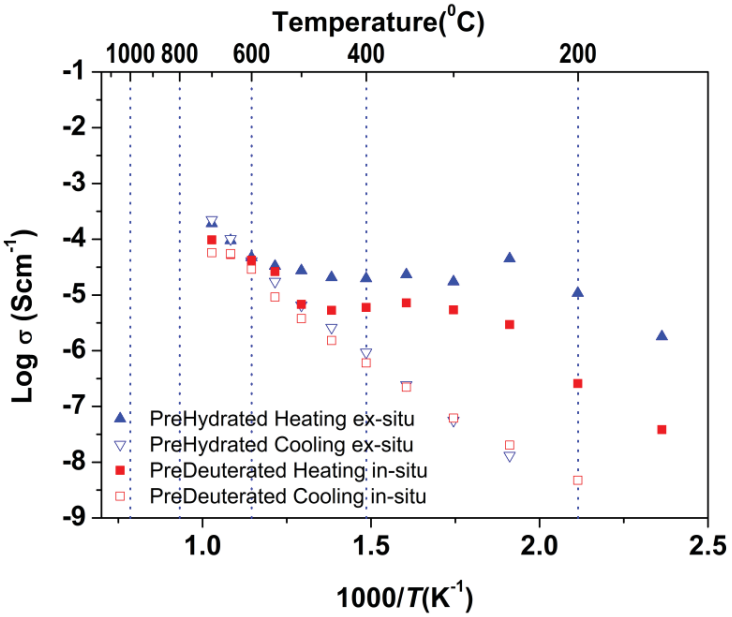

Figure 17: *In-situ* conductivity data of pre-deuterated sample compared to *ex-situ* pre-hydrated sample data collected by Ahmed *et al.*[47].

The deuteron conductivity of $BaZr_{0.5}In_{0.5}O_{2.75}$ for T ≥ 823 K follows the same trend on for heating and cooling as the measured lattice parameter at those temperatures. At ~500 K to ~800 K a characteristic plateau like region for proton conductors exists, whereby the highly mobile protons/deuterons are leaving the structure[46]. This is once again matched by the behavior of the simultaneously measured lattice parameter (figure 16) at ~500K to ~800 K. The herein reported conductivity, plotted in figure 17, was less than the protonic conduction previously reported by Ahmed *et al.*[47], by an order of magnitude lower at 523 K (D_2O σ = 2.94×10^{-6} Scm^{-1} vs. H_2O σ = 4.49×10^{-5} Scm^{-1}). This is primarily due to the isotope effect [51] from using D_2O for humidification instead of H_2O and the fact that the samples were inherently different in terms of microstructure (not the same batch of pellets).

4.3 The Structure and Protonic Conduction of Scandium Doped $BaSnO_3$

$BaSn_{1-x}Sc_xO_{3-\delta}$ was synthesized for the series x = 0, 0.1, 0.2, 0.3, 0.4, 0.5 (BS0, BS1, BS2, BS3, BS4, BS5 respectively) by the solid state synthesis route. The samples were characterized by XRPD, EIS, NPD, and ^{119}Sn-NMR techniques. All samples except for BS5 were found to be X-ray pure. Room temperature neutron powder diffraction (NPD) data was collected for BS2, BS3, and BS4 dry and hydrothermally deuterated samples. However on inspection of the NPD plots, peaks belonging to Sc_2O_3 were observed for all the samples except for BS0 and the deuterated BS4 sample. Hence the Deuterated BS4 sample was used to locate the deuteron site in the unit cell. Rietveld refinements were made on the NPD data and Fourier difference maps plotted to investigate missing positive scattering for the Deuteron site. There was evidence of the presence of a $BaSnO_3$ phase in the samples containing Sc_2O_3. The refined cell parameters for the $BaSnO_3$ phase in BS2 deuterated BS3 dry samples were identical to that of the BS0 sample within experimental uncertainty while that of the BS3 deuterated sample was only marginally larger. The $BaSnO_3$ component was not included in the rietveld refinements for dry BS2 samples as it did not yield sensible phase fractions due to the peaks for the doped phase and the undoped $BaSnO_3$ phase being too close together.

The occupancies of the Sn/Sc sites were recalculated in a spread sheet from the obtained phase fractions after each refinement cycle in a cyclic manner until the change in occupancy stabilized. The oxygen site occupancy for deuterated samples was set to 1 for BS2 and BS3 but deuterons were not included in their refinement models.

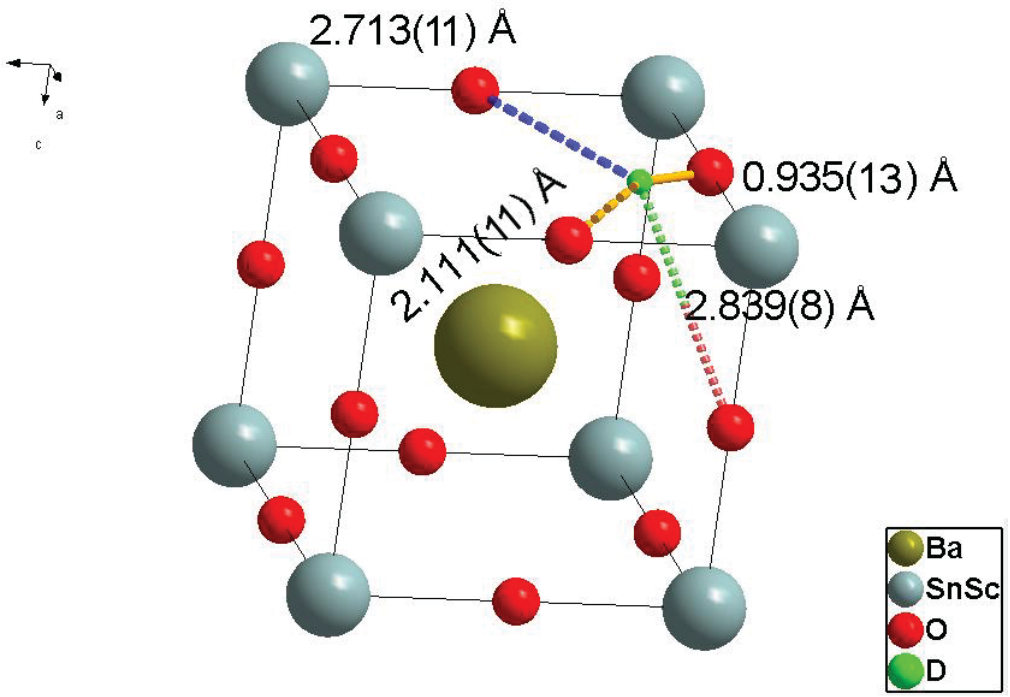

Figure 18: The unit cell of $BaSn_{0.6}Sc_{0.4}O_{2.8}(D_2O)_{0.2}$ showing bond arrangements, distances and the deuteron site at 24*k* (0.584(2), 0.208(3), 0).

The refined O-D bond (*fig. 19*) distance of 0.935(13) Å is comparable to literature values for similar systems [50, 52, 53] and the hydrogen bond distance was 2.111(11) Å, a reasonable value for facilitating a jump of the deuteron to the next site. The 24*k* site of the deuteron has 8 equivalent positions about each oxygen site and is descriptive of the deuteron being displaced towards a neighbouring site in favour of hydrogen bonding in agreement with the theoretical findings of Shi *et al.*[54] on the Indium doped $BaZrO_3$ system experimental findings of Ahmed *et al.*[50] on of $BaZr_{0.5}In_{0.5}O_{2.75}$.The protonic conductivity was found to increase with Scandium doping and levelled out at *x ~0.3-04* before falling off.

5 Conclusion and Future Work

In Paper I the importance of the various synthesis and processing techniques of $BaZr_{0.5}In_{0.5}O_{2.75}$ have been elaborated in relation to the microstructure which has been shown to affect the behavior of conductivity. The achievement of a high level of densification via SPS is demonstrated and the need for long soaking times to achieve large grains is demonstrated. However the unexpected higher bulk conductivity for under wet Ar for the smaller grained SPS sample needs to be further investigated.

Paper II has demonstrated the *in-situ* experimental characterization facilities at ISIS developed in partnership with Chalmers using a well-known system of $BaZr_{0.5}In_{0.5}O_{2.75}$. The additional new insight into the hydration behavior with respect to temperature and the structural thermal parameters of the oxygen anion has been gained in this work.

A detailed understanding on Sc-doped $BaSnO_3$ (paper III) has been developed and the deuteron site located and a detailed atomic model has been obtained. The contrast between the various probing techniques such as XRPD, NPD and NMR and the complimentary information they provide is demonstrated.

In the future fluorite-pyrochlore O^{2-} conducting systems will be investigated with a special attention paid to what happens to the structure transition and its associated increase in oxide ion conduction. $Y_2(Ti_{1-x}Zr_x)_2O_7$ and $Ce_2Zr_2O_7$ will be studied. The latter, is used extensively in the automotive industry in catalytic converters will be studied as a function of $p(O_2)$ using the gas flow cell described in paper II.

Acknowledgements

I would like to express my heartfelt gratitude and thanks to my supervisor, Professor Sten Eriksson for his unwavering support, guidance, teaching, encouragement and trust before and during the duration of my work. Together with Professor Emeritus, Oliver Lindqvist, I express many thanks in enabling my studentship at the Environmental Inorganic Chemistry division at Chalmers University of Science and Technology.

Many thanks to my co-supervisors Associate Professor Stefan Norberg, Associate Professor Chris Knee and Dr. Istaq Ahmed for their invaluable discussions suggestions and input into my works. I express sincere gratitude to Dr. Istaq Ahmed for being a mentor and a role model.

Sincere appreciations to members of the oxide group both current and former, including Dr. Annika Eriksson, Habibur Rahman and Stefan Saxin for their support and cooperation in the office and in the labs. Special thanks to Professor Vratislav Langer and technical support personnel, Roger Saghdahl and Esa Väänänen without whom my experiments would not be possible.

I also thank Professor Elisabet Ahlberg and Patrick Steegstra of the Electrochemistry group at Gothenburg University for their expert advice, collaboration and cooperation in their lab.

I thank my collaborators Dr. Steve Hull of the ISIS facility in Oxford, U.K for his expertise in Neutron diffraction and Dr. Lucienne Buannic, Dr. Frédéric Blanc and Clare P. Grey of Stony Brook University in N.Y, USA and University of Cambridge, U.K. for their invaluable input in NMR studies.

I deeply acknowledge the Swedish research council for the financial support in my work and the possibility of obtaining neutron beam time.

I'm thankful to my wife, Wanja, for bearing with me during the writing of the thesis for the unpredictable working hours and to my family back at home for having unshakable faith in me.

Francis Kinyanjui

Gothenburg, May 2012

Appendix A

Table 1: Key descriptors of the *in-situ* humidification cell

	Description
1	*Gas Outlet*
2	*Quartz tube*
3, 10	*Oxygen sensor*
4	*Oxygen sensor controller*
5	*Dry gas inlet*
6	*Wet gas inlet*
7	*Gas humidifier*
8	*Gas mixing setup*
9	*Temperature controller*
10	*Sample*
11	*Quartz fritz*
12	*Thermocouple*
13	*Gas inlet*
14	*Vanadium heat shields (3)*
15	*Vanadium heating element*

Table 2: Key descriptors of the *in-situ* impedance spectroscopy cell

	Description
1	*Solartron 1260*
2	*Gas Outlet*
3	*Quartz tube*
4	*Thermocouple*
5-7	*Heat radiation baffles*
8, 10	*Boron nitride (BN) shielding*
9	*Sample*
11	*Vanadium heat shields (3)*
12	*Platinum electrode*
13	*Vanadium heating element*
14	*BN shielding for electrode*
15	*Gas inlet*
16	*Gas mixing setup*
17	*Temperature controller*

References

[1] B. C. H. Steele and A. Heinzel, "Materials for fuel-cell technologies," *Nature,* vol. 414, pp. 345-352, 2001.

[2] K. D. Kreuer, "PROTON-CONDUCTING OXIDES," *Annual Review of Materials Research,* vol. 33, pp. 333-359, 2003.

[3] T. Norby, "Solid-state protonic conductors: principles, properties, progress and prospects," *Solid State Ionics,* vol. 125, pp. 1-11, 1999.

[4] U. DoE, "Comparison of Fuel Cell Technologies," Apr 01 2011.

[5] T. H. Etsell and S. N. Flengas, "Electrical properties of solid oxide electrolytes," *Chemical Reviews,* vol. 70, pp. 339-376, Jul 1970.

[6] N. Q. Minh, "Ceramic Fuel Cells," *Journal of the American Ceramic Society,* vol. 76, pp. 563-588, Apr 1993.

[7] T. Norby, "The promise of protonics," *Nature,* vol. 410, pp. 877-878, 2001.

[8] D. A. Boysen, T. Uda, C. R. I. Chisholm, and S. M. Haile, "High-Performance Solid Acid Fuel Cells Through Humidity Stabilization," *Science,* vol. 303, pp. 68-70, January 2, 2004 2004.

[9] S. M. Haile, D. A. Boysen, C. R. I. Chisholm, and R. B. Merle, "Solid acids as fuel cell electrolytes," *Nature,* vol. 410, pp. 910-913, 2001.

[10] I. Ahmed, S. G. Eriksson, E. Ahlberg, C. S. Knee, M. Karlsson, A. Matic, D. Engberg, and L. Börjesson, "Proton conductivity and low temperature structure of In-doped BaZrO3," *Solid State Ionics,* vol. 177, pp. 2357-2362, 2006.

[11] I. Ahmed, C. S. Knee, S. G. Eriksson, E. Ahlberg, M. Karlsson, A. Matic, and L. Börjesson, "Proton conduction in perovskite oxide BaZr0.5Yb 0.5O3-δ prepared by wet chemical synthesis route," *Journal of The Electrochemical Society,* vol. 155, pp. P97-P102, 2008.

[12] I. Ahmed, F. G. Kinyanjui, P. Steegstra, Z. J. Shen, S. G. Eriksson, and M. Nygren, "Improved proton conductivity in spark-plasma sintered dense ceramic BaZr0.5 In0.5 O3-δ," *Electrochemical and Solid-State Letters,* vol. 13, pp. B130-B134, 2010.

[13] S. Tao and J. T. S. Irvine, "Conductivity studies of dense yttrium-doped BaZrO3 sintered at 1325°C," *J. Solid State Chem.,* vol. 180, pp. 3493-3503, Dec 2007.

[14] M. M. Bucko, "Ionic conductivity of the yttria-stabilized-zirconia nanomaterials," pp. 543-546.

[15] P. Babilo and S. M. Haile, "Enhanced Sintering of Yttrium-Doped Barium Zirconate by Addition of ZnO," *Journal of the American Ceramic Society,* vol. 88, pp. 2362-2368, Sep 2005.

[16] O. J. Durá, M. A. López de la Torre, L. Vázquez, J. Chaboy, R. Boada, A. Rivera-Calzada, J. Santamaria, and C. Leon, "Ionic conductivity of nanocrystalline yttria-stabilized zirconia: Grain boundary and size effects," *Physical Review B,* vol. 81, Jun 2010.

[17] K. D. Kreuer, S. Adams, W. Münch, A. Fuchs, U. Klock, and J. Maier, "Proton conducting alkaline earth zirconates and titanates for high drain electrochemical applications," *Solid State Ionics,* vol. 145, pp. 295-306, 2001.

[18] D. Ruzmetov, Y. Seo, L. J. Belenky, D. M. Kim, X. Ke, H. Sun, V. Chandrasekhar, C. B. Eom, M. S. Rzchowski, and X. Pan, "Epitaxial Magnetic Perovskite Nanostructures," *Advanced Materials,* vol. 17, pp. 2869-2872, Dec 05 2005.

[19] R. J. H. Voorhoeve, D. W. Johnson, J. P. Remeika, and P. K. Gallagher, "Perovskite Oxides: Materials Science in Catalysis," *Science,* vol. 195, pp. 827-833, Apr 04 1977.

[20] Y. Takeda, N. Imanishi, R. Kanno, T. Mizuno, H. Higuchi, O. Yamamoto, and M. Takano, "Oxide ion conductivity in perovskite type Sr2ScAlO5 and related compounds," *Solid State Ionics,* vol. 53-56, pp. 748-753.

[21] T. Scherban, W. K. Lee, and A. S. Nowick, "Bulk protonic conduction in Yb-doped SrCeO3 and BaCeO3," *Solid State Ionics,* vol. 28-30, pp. 585-588, 1988.

[22] X. Chu, "Dilute CH3SH-sensing characteristics of BaSnO3 thick film sensor," *Materials Science and Engineering B,* vol. 106, pp. 305-307, 2004.

[23] U. Lampe, J. Gerblinger, and H. Meixner, "NITROGEN-OXIDE SENSORS BASED ON THIN-FILMS OF BASNO3," *Sensors and Actuators B: Chemical,* vol. 26, pp. 97-98, Jun 1995.

[24] J. Cerdà, J. Arbiol, G. Dezanneau, R. Díaz, and J. R. Morante, "Perovskite-type BaSnO3 powders for high temperature gas sensor applications," *Sensors and Actuators B: Chemical,* vol. 84, pp. 21-25, 2002.

[25] "Characterization of BaSnO3-based ceramics-Part 1. Synthesis, processing and microstructural development," pp. 1-12, Jun 25 1998.

[26] Y. Wang, A. Chesnaud, E. Bevillon, J. Yang, and G. Dezanneau, "Synthesis, structure and protonic conduction of $BaSn_{0.875}M_{0.125}O_{3-\delta}$ (M = Sc, Y, In and Gd)," *International Journal of Hydrogen Energy,* vol. 36, pp. 7688-7695, 2011.

[27] S. Upadhyay and P. Kavitha, "Lanthanum doped barium stannate for humidity sensor," *Materials Letters,* vol. 61, pp. 1912-1915, 2007.

[28] É. Bévillon, G. Geneste, A. Chesnaud, Y. Wang, and G. Dezanneau, "Ab initio study of La-doped BaSnO3 proton conductor," *Ionics,* vol. 14, pp. 293-301, 2008.

[29] R. Glöckner, M. S. Islam, and T. Norby, "Protons and other defects in BaCeO3: a computational study," *Solid State Ionics,* vol. 122, pp. 145-156, Oct 1999.

[30] I. Ahmed, S. M. H. Rahman, P. Steegstra, S. T. Norberg, S. G. Eriksson, E. Ahlberg, C. S. Knee, and S. Hull, "Effect of co-doping on proton conductivity in perovskite oxides BaZr 0.9In0.05M0.05O3-δ (M = Yb3+ or Ga3+)," *International Journal of Hydrogen Energy,* vol. 35, pp. 6381-6391, 2010.

[31] I. Ahmed, F. G. Kinyanjui, S. M. H. Rahman, P. Steegstra, S. G. Eriksson, and E. Ahlberg, "Proton conductivity in mixed b-site doped perovskite oxide ba Zr 0.5 In0.25 Yb0.25 O3-δ," *Journal of The Electrochemical Society,* vol. 157, pp. B1819-B1824, 2010.

[32] K.-D. Kreuer, "Proton Conductivity: Materials and Applications," *Chemistry of Materials,* vol. 8, pp. 610-641, 1996.

[33] T. Schneller and T. Schober, "Chemical solution deposition prepared dense proton conducting Y-doped BaZrO3 thin films for SOFC and sensor devices," *Solid State Ionics,* vol. 164, pp. 131-136, Nov 2003.

[34] U. Anselmi-Tamburini, M. T. Buscaglia, M. Viviani, M. Bassoli, C. Bottino, V. Buscaglia, P. Nanni, and Z. A. Munir, "Solid-state synthesis and spark plasma sintering of submicron $BaY_xZr_{1-x}O_{3-x/2}$ (x=0, 0.08 and 0.16) ceramics," *Journal of the European Ceramic Society,* vol. 26, pp. 2313-2318, 2006.

[35] T. E. Engin, A. V. Powell, R. Haynes, M. A. H. Chowdhury, C. M. Goodway, R. Done, O. Kirichek, and S. Hull, "A high temperature cell for simultaneous electrical resistance and neutron diffraction measurements," *Review of Scientific Instruments,* vol. 79, p. 095104, 2008.

[36] S. Hull, R. I. Smith, W. I. F. David, A. C. Hannon, J. Mayers, and R. Cywinski, "The Polaris powder diffractometer at ISIS," *Physica B: Condensed Matter,* vol. 180-181, pp. 1000-1002, 1992.

[37] H. Kohlmann, B. Bertheville, T. Hansen, and K. Yvon, "High-pressure synthesis of novel europium magnesium hydrides* 1," *Journal of Alloys and Compounds,* vol. 322, pp. 59-68.

[38] R. J. Cava, A. W. Hewat, E. A. Hewat, B. Batlogg, M. Marezio, K. M. Rabe, J. J. Krajewski, W. F. Peck Jr, and L. W. Rupp Jr, "Structural anomalies, oxygen ordering and superconductivity in oxygen deficient Ba2YCu3Ox," *Physica C: Superconductivity,* vol. 165, pp. 419-433.

[39] D. E. Cox and A. W. Sleight, "Crystal structure of Ba2Bi3+Bi5+O6," *Solid State Comm.,* vol. 19, pp. 969-973.

[40] B. T. M. Willis and C. J. Carlile, *Experimental neutron scattering*. Oxford; New York: Oxford University Press, 2009.

[41] H. Rietveld, "A profile refinement method for nuclear and magnetic structures," *Journal of Applied Crystallography,* vol. 2, pp. 65-71, 1969.

[42] L. B. McCusker, R. B. Von Dreele, D. E. Cox, D. Louer, and P. Scardi, "Rietveld refinement guidelines," *Journal of Applied Crystallography,* vol. 32, pp. 36-50, 1999.

[43] R. B. V. D. A C Larson, "General Structure Analysis System (GSAS)," *Los Alamos National Laboratory Report,* vol. LAUR pp. 86-748.

[44] R. Haynes, S. T. Norberg, S. G. Eriksson, M. A. H. Chowdhury, C. M. Goodway, G. D. Howells, O. Kirichek, and S. Hull, "New high temperature gas flow cell developed at ISIS," *Journal of Physics: Conference Series,* vol. 251, p. 012090, Dec 16 2010.

[45] U. ANSELMITAMBURINI, M. BUSCAGLIA, M. VIVIANI, M. BASSOLI, C. BOTTINO, V. BUSCAGLIA, P. NANNI, and Z. MUNIR, "Solid-state synthesis and spark plasma sintering of submicron BaYxZr1−xO3−x/2 (x=0, 0.08 and 0.16) ceramics," *Journal of the European Ceramic Society,* vol. 26, pp. 2313-2318, 2006.

[46] I. Ahmed, S. G. Eriksson, E. Ahlberg, C. S. Knee, P. Berastegui, L. G. Johansson, H. Rundlöf, M. Karlsson, A. Matic, L. Börjesson, and D. Engberg, "Synthesis and structural characterization of perovskite type proton conducting BaZr1-xInxO3-δ (0.0 ≤ x ≤ 0.75)," *Solid State Ionics,* vol. 177, pp. 1395-1403, 2006.

[47] I. Ahmed, S. G. Eriksson, E. Ahlberg, and C. S. Knee, "Influence of microstructure on electrical properties in BaZr0.5In0.5O3 - δ proton conductor," *Solid State Ionics,* vol. 179, pp. 1155-1160, 2008.

[48] H. Iwahara, "Proton Conduction in Sintered Oxides Based on BaCeO3," *Journal of The Electrochemical Society,* vol. 135, p. 529, 1988.

[49] A. POTTER and R. BAKER, "Impedance studies on Pt|SrCe0.95Yb0.05O3|Pt under dried and humidified air, argon and hydrogen," *Solid State Ionics,* vol. 177, pp. 1917-1924, Oct 15 2006.

[50] I. Ahmed, C. S. Knee, M. Karlsson, S. G. Eriksson, P. F. Henry, A. Matic, D. Engberg, and L. Börjesson, "Location of deuteron sites in the proton conducting perovskite BaZr0.50In0.50O3−y," *Journal of Alloys and Compounds,* vol. 450, pp. 103-110, 2008.

[51] N. Bonanos, "Transport properties and conduction mechanism in high-temperature protonic conductors," *Solid State Ionics,* vol. 53-56, pp. 967-974.

[52] E. Kendrick, K. S. Knight, M. S. Islam, and P. R. Slater, "Structural studies of the proton conducting perovskite 'La0.6Ba0.4ScO2.8'," *Solid State Ionics,* vol. 178, pp. 943-949, 2007.

[53] T. I. Takanori Nagasaki, Masahito Yoshino, Kouta Iwasaki,Shinya Shiotani, Hiroshi Fukazawa, Naoki Igawa ,Yoshinobu Ishii, "Location of Deuterium Atoms in BaZr0.5In0.5O2.75 by Neutron Powder Diffraction," *Journal of Nuclear Science and Technology,* vol. Supplement 6, pp. 122-127, September 2008 2008.

[54] C. Shi, M. Yoshino, and M. Morinaga, "First-principles study of protonic conduction in In-doped AZrO3 (A=Ca, Sr, Ba)," *Solid State Ionics,* vol. 176, pp. 1091-1096, 2005.